Nanoscale

Thermal stability of self-assembled ordered three-phase Au-BaTiO3-ZnO nanocomposite thin films via in situ heating in TEM

Journal:	*Nanoscale*
Manuscript ID	NR-ART-08-2020-006115.R1
Article Type:	Paper
Date Submitted by the Author:	27-Oct-2020
Complete List of Authors:	Misra, Shikhar; Purdue University Zhang, Di; Purdue University, School of Materials Engineering Lu, Ping; Sandia National Laboratories, Wang, Haiyan; Purdue University System, MSE; Neil Armstrong Engineering Building

Thermal stability of self-assembled ordered three-phase Au-$BaTiO_3$-ZnO nanocomposite thin films via *in situ* heating in TEM

Shikhar Misra,[a] Di Zhang,[a] Ping Lu,[b] Haiyan Wang[a,c,*]

[a]School of Materials Engineering, Purdue University, West Lafayette, Indiana 47907, United States
[b]Sandia National Laboratory, Albuquerque, New Mexico 87185, United States
[c]School of Electrical and Computer Engineering, Purdue University, West Lafayette, Indiana 47907, United States

[*]Author to whom correspondence should be addressed. E-mail: hwang00@purdue.edu

Keywords:

in situ heating, *ex situ* heating, thermal stability, metamaterial, thin films, vertically aligned nanocomposite

Abstract

Thermal stability of oxide-metal nanocomposites is important for designing practical devices for high temperature applications. Here, we study the thermal stability of the self-assembled ordered three-phase Au-$BaTiO_3$-ZnO nanocomposite by both the *ex situ* annealing in air and vacuum conditions, and by *in situ* heating in TEM in vacuum. The study reveals that the variation of the annealing conditions greatly affects the resulted microstructure and the associated dominant diffusion mechanism. Specifically, Au nanoparticles show coarsening upon air annealing while Au and Zn either form a solid solution, with Zn atomic percentage less than 10% or undergo reverse Vapor-Liquid-Solid (VLS) mechanism upon vacuum annealing. The distinct microstructures obtained also show different permittivity response in the visible and near-infrared region, while retaining their hyperbolic dispersion characteristics enabled by their highly anisotropic structures. Such *in situ* heating study in TEM provides critical information of microstructure evolution, growth mechanisms at nanoscale, and thermal stability of the multi-phase nanocomposites for future electronic device applications.

Introduction

Metamaterials offer extensive opportunities for engineering the light-matter interaction, ideal for achieving exotic optical properties including optical magnetism,[1] negative refraction,[2] and hyperbolic dispersion[3] which have potential applications in the field of optical computing, cloaking and sub-diffraction imaging. One such class of metamaterials is hyperbolic metamaterial (HMM), which have a highly anisotropic structure, composed of metal and dielectric units, and support the propagation of high wavevectors.[4,5] Recently, several two-phase metal-dielectric self-assembled nanocomposites, as vertically aligned or in a layer-by-layer stacking have been shown to exhibit hyperbolic dispersion.[6–8] Beyond the two-phase nanocomposite structures, a greater design flexibility can be achieved by incorporating a third phase through the three-phase nanocomposite design.[9–11] The three phase nanocomposites offer great opportunities for a wide range of material selection and functionality coupling for developing next generation integrated electronic and photonic devices. A careful selection of materials and functionalities can further help in the spatial ordering of the three phases which is essential for metamaterial properties. Recently, a self-assembled ordered three-phase nanocomposite of Au-$BaTiO_3$-ZnO has been demonstrated as a hyperbolic metamaterial in the visible and near-infrared wavelength region.[9]

Thermal stability of plasmonic and hyperbolic optical structures is critical for applications such as in heat-assisted magnetic recording, biosensors, photothermal therapy, and thermophotovoltaics.[12–17] In general, metallic based plasmonic and hyperbolic nanostructures have poor thermal stability and limited durability, which leads to property degradation. With increasing temperatures, different physical processes become active such as enhanced diffusion, phase change and crystallinity change, that alter their physical properties. Previously, thermal stability study in TEM has been performed on two phase oxide-oxide (BFO-SmO) based nanocomposites, which demonstrated stability up to 600°C and pore formation above 750°C.[18] In general dielectrics are more thermally stable having high melting points as compared to metals. Therefore, the oxide-metal nanocomposites offer unique opportunity in achieving enhanced thermal stability as compared to metallic films. Among them, the self-assembled ordered three-phase metamaterial system offer an exciting path forward towards increased multifunctionalities. Therefore, exploring the complex phase interactions, phase change, growth mechanisms and thermal stability of these complex three-phase system, is extremely critical for plasmonics-based refractory applications.

Recently, in-situ heating studies in TEM have also been demonstrated in oxide-metal

system (Au-BTO), which demonstrated high thermal stability upto 600°C.[19] In this work, thermal stability studies were performed on the ordered three phase Au-$BaTiO_3$-ZnO sample by both the *ex situ* annealing in air and vacuum environment, and the *in situ* annealing in TEM, to investigate the microstructural change. $BaTiO_3$ (BTO) matrix serves as a thermally stable matrix[19] whereas Au and ZnO undergo microstructural changes at elevated temperatures. The heating profiles used for air and vacuum annealing are illustrated in **Figure 1** which allow the exploration of the growth mechanism. The samples were heated to 650°C *ex situ* in air and vacuum for 1 hr. Interestingly, changing the annealing environment activates a different growth mechanism, leading to the formation of very distinct microstructures. The sample was also heated *in situ* in TEM under vacuum to study the interfacial effects between Au and ZnO. The optical properties of all the three samples are also compared and correlated to their microstructures. Varying the annealing conditions provides an interesting approach to achieve microstructure and property tuning in oxide-metal nanocomposite systems.

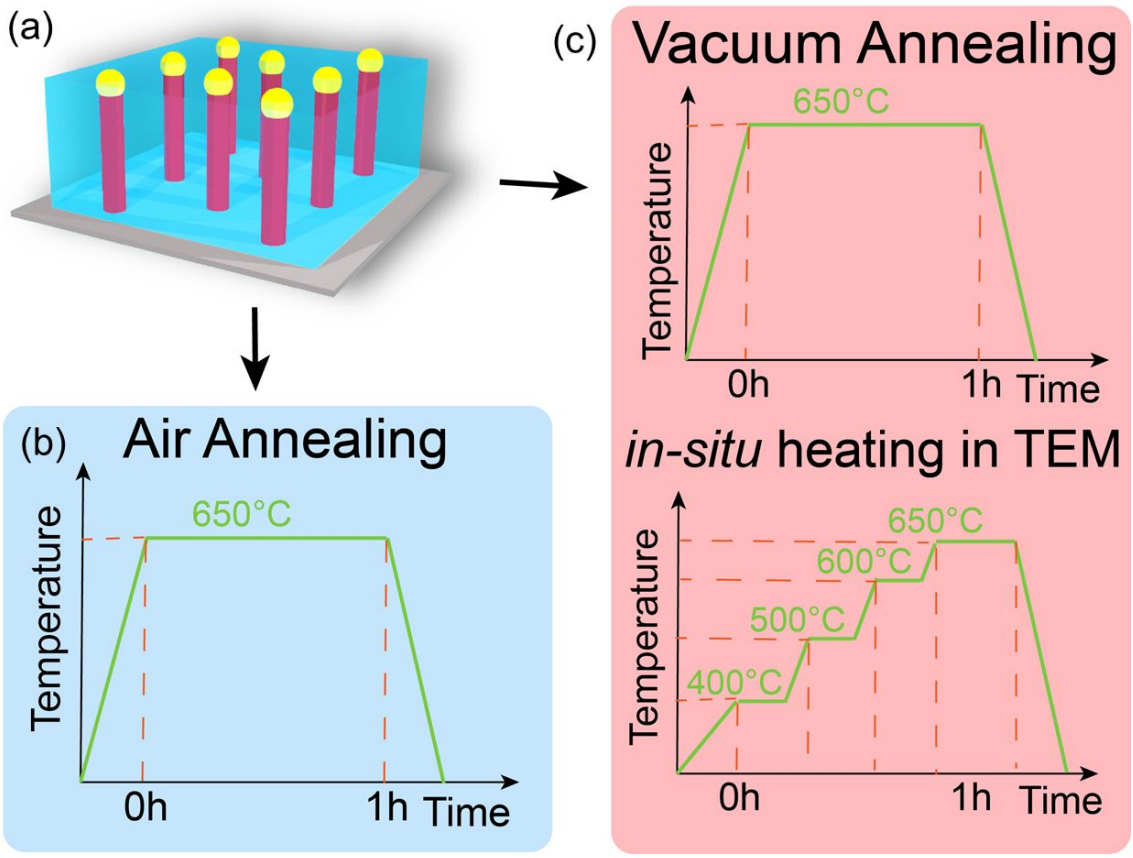

Figure 1. Schematic illustration of the (a) ordered three-phase Au-$BaTiO_3$-ZnO nanocomposite. Heating profiles showing the (b) *ex situ* annealing in air, (c) in vacuum, and during *in situ* heating in TEM to investigate the thermal stability of the nanocomposite thin film.

Results and Discussion

To study the thermal stability of the three-phase nanocomposite, the sample was annealed at 650°C, both in air and in vacuum for 1 hr. 650°C was chosen specifically since it is close to the growth temperature, which was set at 700°C and due to the experimental limitation of the in-situ heating holder. The X-ray diffraction (XRD) θ-2θ scans (Supplementary Information S1) of all the three-phase samples show that the BTO phase remains textured in the [00l] direction. The splitting in the BTO peak arises from the two different BTO layers, in the Au-BTO and the BTO-ZnO films, respectively. Such peak splitting can be attributed to the lattice relaxation in the two layers. The BTO present in the upper BTO-ZnO layer undergoes strain relaxation since it gets deposited onto BTO, instead of STO, as the effective substrate. However, upon annealing the sample in vacuum, the ZnO (0002) peak disappears. To further confirm the absence of the ZnO phase upon vacuum

annealing, Raman spectroscopy was conducted on the samples after annealing in air and vacuum. The Raman signal from ZnO is relatively weak due to its very small diameter (~7.6 nm). The Raman shift, presented in Supporting Information, Figure S2 shows that the two samples share similar features overall. However, the absence of the ZnO peak at 414 cm^{-1} and ~1100 cm^{-1} after vacuum annealing confirms that the ZnO phase is absent.

To gain a better understanding of the growth mechanism, scanning transmission electron microscopy (STEM) was performed on the samples. **Figure 2** compares the sample morphology of the as-deposited sample and after annealing it in air and vacuum for 1hr. The microstructure of the as-deposited sample (shown in Figure 2a) is similar to the one that has been reported earlier.[9] It shows the presence of Au NPs capping the ZnO nanowires, embedded inside the BTO matrix. Figure 2b shows the microstructure and phase distribution after annealing the sample in air at 650°C for 1hr. Overall, the morphology looks quite similar with Au and ZnO pillars arranged in an ordered fashion. The length and diameter of the Au and ZnO pillars are approximately the same (~7.2 nm and ~7.6 nm, respectively). However, the size of the Au NPs capping the ZnO NWs is very different. The size of the Au NPs increases from ~10nm to ~16nm after post-growth annealing in air. Besides, the number of Au NPs capping the ZnO NWs significantly reduces after annealing. Such increase in the size of the Au NPs size suggests the diffusion of Au from smaller particles to the larger ones (Ostwald ripening) along the BTO surface to reduce the total particle surface area. During the post-growth anneal, coarsening of the Au NPs make the particles transition from a faceted shape to a round shape. The Au NP size increases from 9.1±1.9 nm before annealing to 16.8±5.0 nm after annealing due to the Ostwald ripening. In contrast, the particles embedded inside

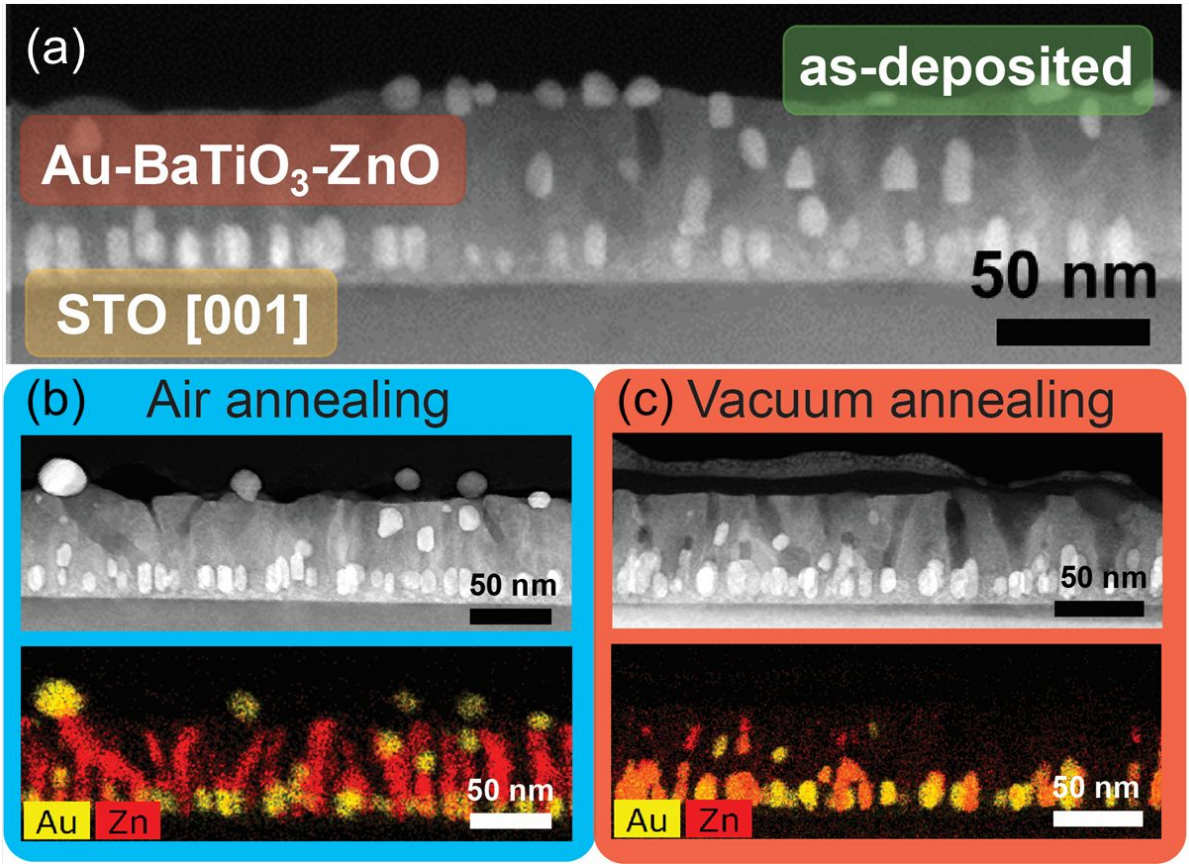

Figure 2. *Ex situ* annealing of the ordered three-phase Au-$BaTiO_3$-ZnO nanocomposite. (a) Cross-sectional STEM image of the as-deposited Au-$BaTiO_3$-ZnO nanocomposite, Cross-sectional STEM image and the corresponding EDS map after *ex situ* annealing in (b) air and (c) vacuum

the BTO matrix do not undergo Ostwald ripening, maintain their shape and size and are thermally stable during the annealing process. These results confirm that Au can diffuse from one catalyst NP to another NP during equilibrium conditions by migrating along the BTO surface. Further investigation was done by annealing the sample at 650°C in vacuum for 1hr. Figure 2c shows the microstructure and phase distribution after doing vacuum annealing. Surprisingly, the morphology looks completely different on changing the annealing environment. The Au NPs present at the surface reduces significantly after vacuum annealing. EDS mapping also shows the alloying between Au and Zn to form a AuZn solid solution. The oxygen partial pressure required to reduce bulk ZnO to Zn at 650°C is 10^{-25} torr, as calculated from the Ellingham diagram.[20] However, the pressure in furnace and column pressure in TEM was maintained at 10^{-6} torr and 10^{-10} torr before annealing, respectively. The oxygen partial pressure required for the dissociation of bulk ZnO

(above 750°C) has been reported previously as[21]: $\log P_{O2}(Torr) = -\frac{13500}{T} + 8.01$, which gives oxygen partial pressure of 10^{-5} torr at 750°C. It is likely that the ZnO NW still gets reduced to Zn by annealing in vacuum due to the reducing environment created by the low oxygen partial pressure, high temperature, oxygen vacancies, nanostructure formation and impurity carbon as has been reported before.[21–26] Reducing environment increases the oxygen vacancies in ZnO_x, thereby reducing the interfacial energy of Au/ZnO_x due to the miscibility of Au and Zn. Interestingly, Au and Zn forms a solid solution, evident from the EDS mapping showing the elemental distribution in Figure 2c. The phase composition of the AuZn solid solution is discussed in more detail later. Clearly, oxygen pressure plays a critical role in determining the final morphology of the three-phase Au-BTO-ZnO nanocomposite.

In order to gain a further understanding of the growth mechanism of the ordered three phase nanocomposite, the thermal stability of the film was investigated using *in situ* heating in TEM in vacuum. The thickness of the film used for the in-situ heating experiment was ~80nm. The Au and ZnO nanopillar diameter was 10.27±1.15nm and 7.60±1.95nm, respectively, while the aspect ratio of Au NPs capping the ZnO NW was 1.26±0.56. *In situ* heating in TEM was conducted on a cross-section TEM sample with heating from room temperature (RT) to 650°C and the corresponding STEM images were recorded at RT, 400°C, 500°C, 600°C and 650°C. **Figure 3** shows the morphology variation and transformation in four selected Au NPs and pillars. These snapshot images highlight the different aspects of the mechanism at five different temperatures. Figure 3a shows a Au NP capping a ZnO NW, having a facetted surface at room temperature. Upon increasing the temperature to 400°C, the particle starts to have a smoothly curved surface. The curvature of Au-ZnO interface remains as low as possible. The instability arises from the curved surface near the edge of the ZnO NW. Due to the Gibbs-

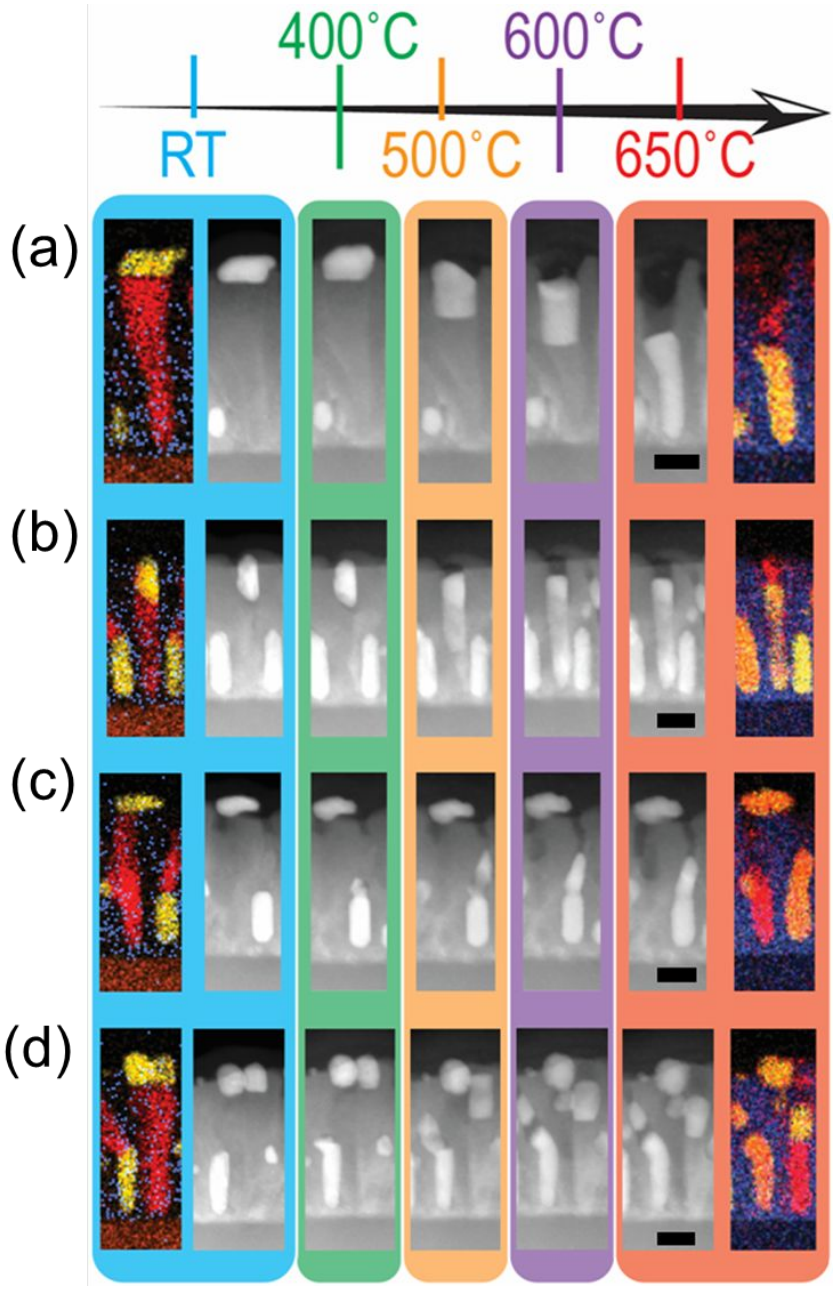

Figure 3. *In situ* heating of Au-$BaTiO_3$-ZnO in TEM. Cross-sectional STEM image along with the initial and final EDS map during the *in situ* heating in TEM from room temperature (RT) to 650°C of the (a)-(d) four selected regions. Scale bar corresponds to 20 nm.

Thomson effect, the solubility of Au in ZnO at this curved surface is greater as compared to the flat surface (Figure S3). Therefore, the Au NP shape starts changing from the corner of the Au-Zn interface. Overall, the particle remains relatively stable up to 400°C. Increasing the temperature to 500°C, increases the diffusion rate of Au into ZnO and they become a liquid alloy phase. The

existence of such eutectic liquid alloy phase below the bulk eutectic temperature is attributed to the nanoscale size effects due to the Gibbs-Thomson effect. Further increasing the temperature to 600°C and 650°C, causes the liquid phase alloy to diffuse through the underlying ZnO phase. It is also possible that the VLS mechanism happens reversibly, specifically, by precipitating the supersaturated ZnO on top of the Au-Zn nanopillar. Similar mechanism is also observed in Figure 3b, wherein the Au NP becomes unstable from its corners and mixes with the ZnO NW, thereby precipitating the supersaturated ZnO NW on top.

Figure 3c shows an isolated Au NP that is slightly in contact with the ZnO NW. Clearly, the Au NP doesn't undergo a major morphology change upon heating. However, its contrast becomes weaker, which is likely due to the Zn diffusion since the image contrast is roughly proportional to Z^2, evident by the EDS mapping. In contrast, the Au pillar, initially in contact with the ZnO pillar becomes a AuZn liquid alloy after heating the sample to 650°C. Similar results are also observed in Figure 3d in which the Au NP diffuses down along ZnO NW while ZnO diffuses to the Au NP to become Au-Zn liquid phase alloy. Therefore, two different mechanisms: (i) reverse VLS, and (ii) formation of AuZn solid solution taking place upon vacuum annealing. The activation of the either mechanism can be attributed to the diameter of the ZnO NW at the Au-ZnO interface at room temperature. When the Au-ZnO interfacial diameter is greater than a critical diameter (~10-11 nm), reverse VLS mechanism takes place and when the Au-ZnO interface is less than the critical diameter, AuZn solid solution formation takes place. Since the smaller ZnO NW has the higher probability of getting reduced to Zn at the same temperature and pressure as compared to the larger ZnO NW, it gets alloyed with Au to form a AuZn solid solution. The morphological changes in the sample take place mainly in two stages. Stage 1 is active up to 400°C, where the microstructure is relatively stable. Further increasing the temperature above 400°C activates stage 2 process, where a rapid microstructural change is seen.

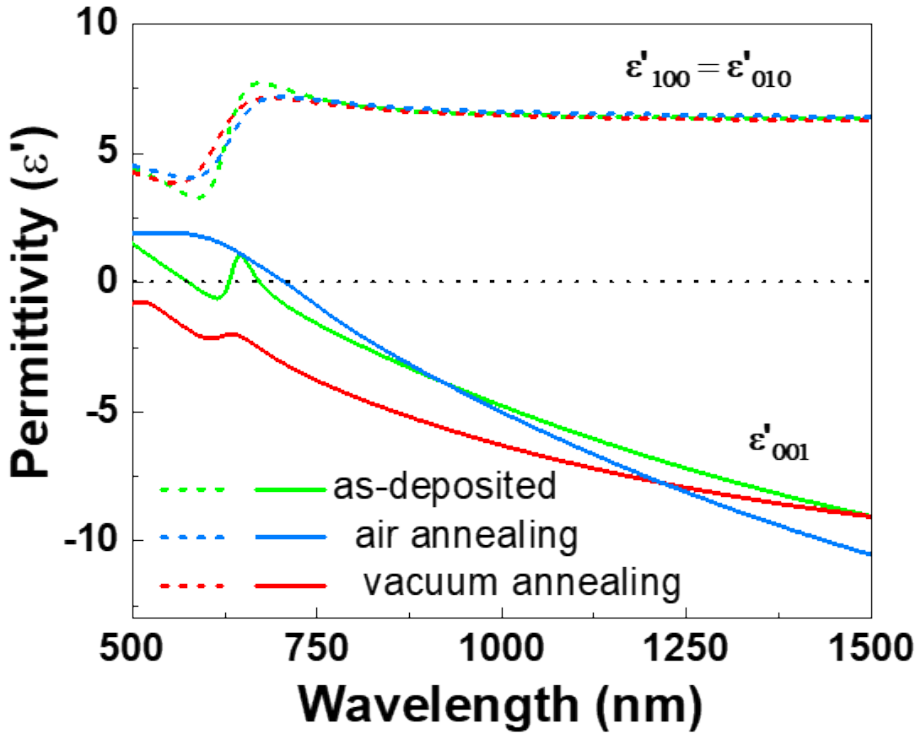

Figure 4. Tunable optical properties. Real part of the in-plane ($\varepsilon'_{100}=\varepsilon'_{010}$) and out-of-plane ($\varepsilon'_{001}$) permittivity for the as-deposited, air-annealed, and vacuum annealed Au-$BaTiO_3$-ZnO thin films.

Optical properties are closely related to the microstructural and morphological change in the sample. The dielectric constant measured from the angular dependent ellipsometry data of the three samples were compared to reveal the effects of the microstructural variation among them. The permittivity was modeled using an anisotropic model through the use of general oscillator models to enforce the Kramers-Kronig consistency. The real part of the in-plane ($\varepsilon'_{\parallel}$) and out-of-plane permittivity ($\varepsilon'_{\perp}$) are plotted in **Figure 4**. Clearly, the $\varepsilon_{\parallel}$ for all the three samples show similar characteristics such as an absorption peak near 600 nm because of the plasmonic absorption by Au and remain positive throughout the wavelength region. Interestingly, the $\varepsilon'_{\perp}$ show a pronounced difference in the visible wavelength region. The as-deposited sample shows a resonant frequency near 600 nm which disappears after air and vacuum annealing. The resonant frequency in the out-of-plane direction possibly arises due to the presence of Au NP capping the ZnO NW as observed earlier.[9] After vacuum annealing, the fraction of Au NPs present largely reduces and the most of

the pillars are Au-Zn alloy which causes the out-of-plane permittivity to become negative throughout the wavelength range. The vacuum annealing leads to the solid solution formation which shows a more metallic behavior in the out of plane direction as compared to the air annealed sample. Nonetheless, all the samples show negative $\varepsilon'_{\perp}$ in the near-infrared wavelength region, thereby retaining the hyperbolic character. Thus, changes in the microstructure directly help tune the optical properties of the three-phase nanocomposite.

The microstructure and phase composition of the three-phase nanocomposite before and after vacuum annealing is further analyzed with the high-resolution STEM images to understand the interface formation mechanism after the VLS growth mechanism. **Figure 5a** presents the HRSTEM image of a BTO-ZnO vertical interface of an as-deposited 3-phase sample. A fast-Fourier transformed (FFT) image (Figure 5b) shows the domain matching relationship along the vertical interface. Several misfit dislocations are present at regular intervals, making the interface as semi-coherent, reducing the vertical strain energy. The BTO-ZnO vertical interface shows two types of domain matching epitaxy (DME): 5 BTO (002) with 4 ZnO (0002) and 6 BTO (002) with 5 ZnO (0002). O atom of ZnO binds alternatively with Ba and Ti atoms of BTO on either side of the ZnO pillar, making the energy of every layer to be similar. Such matching relationship also causes a slight tilt in the ZnO pillar. ZnO growth takes place along [0002] out-of-plane, with two domains growing with a 30° rotation in the in-plane direction with STO. The growth along [0002] out-of-plane exposes its low surface energy planes, specifically, $(11\bar{2}0)$ and $(10\bar{1}0)$, in the vertical direction that is coupled with BTO. Such a growth orientation minimizes the strain and surface energy between the ZnO-BTO and ZnO-STO interfaces.

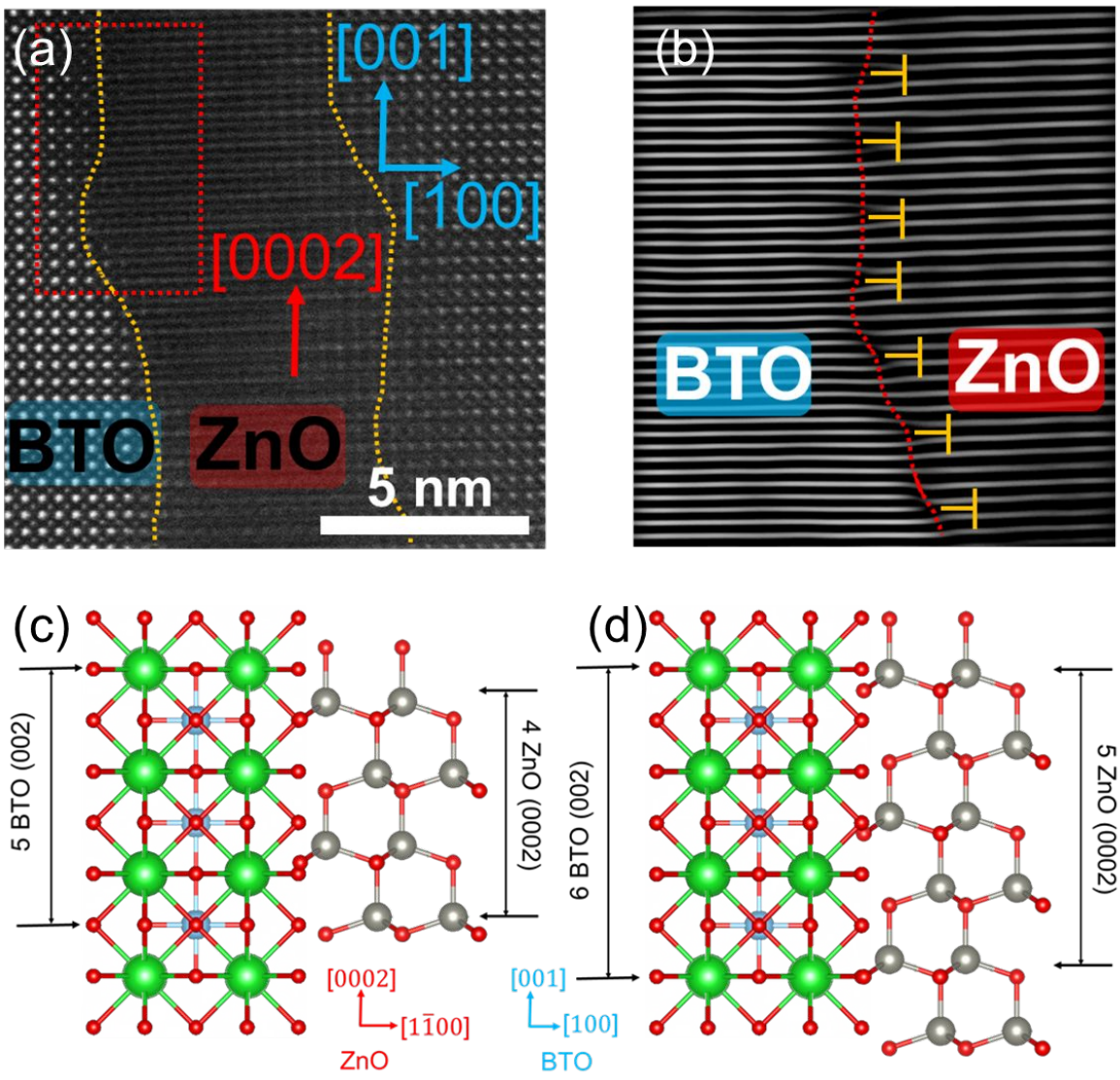

Figure 5. Microstructure of the as-deposited Au-$BaTiO_3$-ZnO nanocomposite. (a) HR-STEM image of the $BaTiO_3$-ZnO vertical interface and its corresponding (b) fourier-transform image showing the presence of dislocations at the $BaTiO_3$-ZnO vertical interface. Schematic illustration showing the two possible domain-matching epitaxy (DME) at the $BaTiO_3$-ZnO vertical interface with (c) 5 BTO (002): 4 ZnO (0002) and (d) 6 BTO (002): 5 ZnO (0002) lattice matching relationship.

Figure 6a-b shows an EDS elemental map of a vacuum annealed sample containing three pillars: the first two are pure Au pillars and the third pillar is a Au-Zn solid solution. The corresponding EDS line-profile is shown in Figure 6c. Clearly, the Zn phase is absent in the first two Au pillars (shown in red) while both Au and Zn are present in the third pillar. Further, using a k factor ($k_{AuL,ZnK}$) of 3.0,[27] the composition of the AuZn alloy is determined to contain less than

10 at.% of Zn, which is within the single phase region of the Au-Zn phase diagram.[28] The Zn atomic concentration was calculated by the Cliff and Lorimer method using x-ray counts of Au L and Zn K obtained from the EDS measurement.[29] Figure S4 (Supplementary Information) shows another EDS line-scan across several pillars, whose compositions are marked in the map. All the AuZn alloys have composition of Zn less than 10 at.%. Interestingly, the solubility of Au in Zn is 33.5 at.% at 683°C and ~12 at.% at room temperature from the bulk Au-Zn phase diagram.[28] The observed low Zn solubility can be attributed to the nanostructured Au and Zn formation, low cooling rate (20°C/min), and the presence of oxygen vacancies, which can cause a deviation of the solidus line from the bulk Au-Zn phase diagram. Figure 6d and 6e compares the atomic resolution STEM image of the Au pillar and $Au_{0.92}Zn_{0.08}$, respectively. The crystal structure of $Au_{0.92}Zn_{0.08}$ is similar to the pure Au, confirming that the AuZn alloy is a solid solution with a FCC structure. The FFT image of the vertical interface between the AuZn solid solution and BTO is shown in Figure 6f. Clearly, no dislocations are formed and the interface remains largely coherent, due to the similar lattice matching relationship between the two phases. Figure 6g shows the HRSTEM image of one ZnO pillar capped by a Au NP after vacuum annealing. In order to compare the vertical interface before and after vacuum annealing, FFT image of the BTO-ZnO interface was analyzed and is presented in Figure 6h. Clearly, Au and BTO show a nearly coherent interface without obvious misfit dislocations while the BTO-ZnO vertical interface shows similar DME as observed before annealing (Figure 5c and 5d), i.e., 5 BTO (002) with 4 ZnO (0002) and 6 BTO (002) with 5 ZnO (0002).

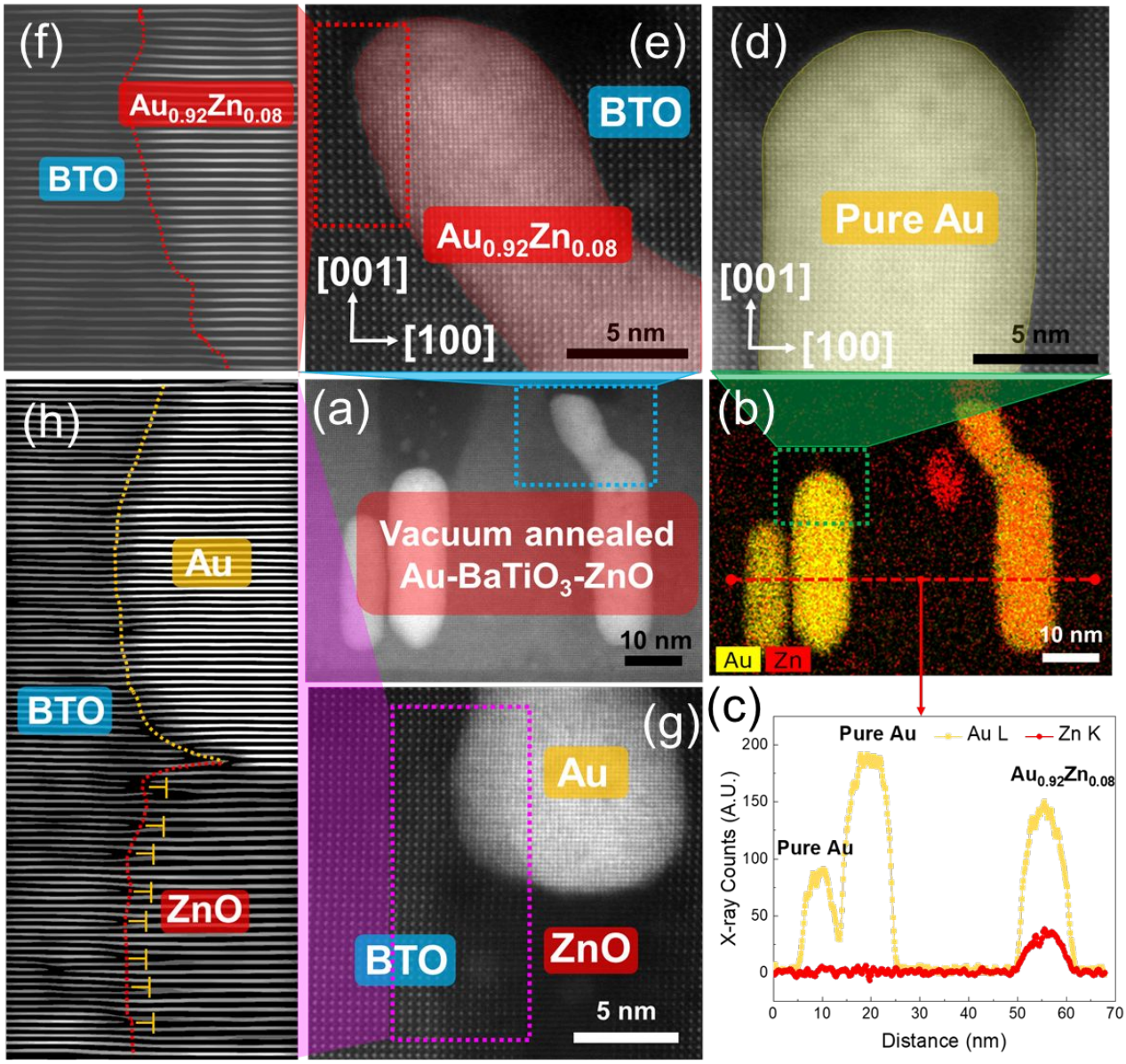

Figure 6. Microstructure of the vacuum-deposited Au-$BaTiO_3$-ZnO nanocomposite. (a) STEM image of the vacuum-annealed Au-$BaTiO_3$-ZnO nanocomposite, (b) its corresponding EDS elemental map and (c) EDS line-scan with the labeled stoichiometry. (d) HR-STEM image of the pure Au pillar and (e) of the pillar with stoichiometry $Au_{0.92}Zn_{0.08}$ with its (f) corresponding fourier-transform image. (g) HR-STEM image of Au-$BaTiO_3$ and $BaTiO_3$-ZnO vertical interface with (h) its corresponding fourier-transform image.

In situ heating experiments in TEM provides useful insights into the phase transformation and structure reconstruction during the annealing of the three-phase Au-BTO-ZnO '*nanoman*' structure. Compared to the thermally stable Au-BTO at 600°C as demonstrated earlier[19], the

experiments here demonstrate the thermal stability of the three-phase structure up to 400°C under vacuum and the interfacial dynamics between the Au and ZnO in nanoscale. It is mainly due to the complex phase interaction between Au and ZnO resulting in either reverse VLS or the formation of Au-Zn solid solution formation. Moreover, the *in situ* heating experiments provide an opportunity to explore the growth mechanisms in other nanocomposite systems, understand their complex phase interactions, trying different annealing environment and realize the factors influencing nanowire growth towards the successful fabrication of nanowire-based devices. Such high thermal stability of these nanocomposites makes them useful in plasmonics-based high temperature applications. Further, their mechanical durability can also be tested using in-situ tensile tests as has been shown previously for Pt thin films and Ag NWs.[30–32]

Conclusions

In summary, the thermal stability of self-assembled ordered three phase Au-$BaTiO_3$-ZnO has been demonstrated by both *ex situ* annealing and *in situ* heating in TEM up to 400°C. The study reveals that different mechanisms are dominant, i.e., Ostwald ripening for annealing in air and reverse VLS and solid solution formation for under vacuum. *In situ* heating experiment in TEM confirms that the ZnO NW diameter at the Au-ZnO interface determines the activation of one of the either mechanism. The three-phase structure remains stable up to 400°C, after which enhanced diffusion starts to take place, leading to a rapid microstructural change. The Zn composition in the AuZn solid solution is less than 10 at.%, thus forming a FCC structure similar to that of pure Au. Such *in situ* heating in TEM provides a powerful means for monitoring the microstructure evolution at nanoscale and complement the existing factors influencing nanowire growth. High temperature stability up to 400°C is helpful for plasmonics-based applications under elevated temperatures.

Experimental Details

Thin Film Growth: The self-assembled three-phase Au-BTO-ZnO nanocomposite thin films were deposited using a two-step growth using a templating method. Initially, an Au-BTO (1:1) thin film was deposited followed by the deposition of BTO-ZnO (1:1) thin film. The thin films were deposited on STO (001) single-crystal substrates using pulsed laser deposition (PLD) (with a KrF excimer laser, Lambda Physik Compex Pro 205, λ = 248 nm). The films were deposited at the

substrate temperature of 700 °C with a laser frequency of 2Hz and 40 mTorr oxygen pressure was maintained during the deposition.

Structural Characterization: The microstructure of the films was investigated by XRD (PANalytical Empyrean XRD), TEM, and high-resolution STEM (FEI TALOS 200X operated at 200 kV). Cross-section TEM samples were prepared using the manual grinding, polishing and thinning process followed by dimpling and ion milling using precision ion polishing system (PIPS II, Gatan). The *in situ* heating experiments were conducted using a furnace type single-tilt *in situ* heating holder (Model 628, Gatan Inc.) with temperature monitoring (Model 1905 Temperature Controller, Gatan Inc.) and water recruiting systems (operates automatically when the holder temperature reaches 500°C). The sample was heated at the rate of 15°C/min and the holding time at each temperature was 10min after which the it was cooled rapidly after reaching to 650°C.

Optical characterization: The dielectric permittivity of the films was measured using spectroscopic ellipsometer (JA Woollam RC2). The measurement was performed at three different angles: 55°, 65°, and 75°. A Raman microscope (Renishaw RM 2000) equipped with a 532 nm green laser was used for the Raman spectroscopy measurements.

Supporting Information

X-Ray Diffraction (XRD), STEM/EDX of vacuum annealed Au-BTO-ZnO nanocomposite, Raman spectroscopy

Acknowledgements

This work was supported by the U.S. Department of Energy, Office of Science, Basic Energy Sciences under Award DE-SC0020077. The TEM/STEM imaging effort was funded by the U.S. National Science Foundation (DMR-1565822 and DMR-2016453). S.M. acknowledges the support from the Bilsland Dissertation Fellowship. D.Z. acknowledges the support from the U.S. Office of Naval Research under contract nos. N00014-17-1-2087 and N00014-20-1-2043 for *in situ* TEM work. Sandia National Laboratories is a multi-program laboratory managed and operated by National Technology and Engineering Solutions of Sandia, LLC., a wholly owned subsidiary of Honeywell International, Inc., for the U.S. Department of Energy's National Nuclear Security Administration under contract DE-NA0003525. This paper describes objective technical results

and analysis. Any subjective views or opinions that might be expressed in the paper do not necessarily represent the views of the U.S. Department of Energy or the United States Government.

References

1. S. Zhang, W. Fan, N. C. Panoiu, K. J. Malloy, R. M. Osgood, and S. R. J. Brueck: Experimental Demonstration of Near-Infrared Negative-Index Metamaterials. *Phys. Rev. Lett.* **95**, 137404 (2005).

2. R. A. Shelby, D. R. Smith, and S. Schultz: Experimental Verification of a Negative Index of Refraction. *Science (80-.).* **292**, 77 (2001).

3. D. R. Smith and D. Schurig: Electromagnetic Wave Propagation in Media with Indefinite Permittivity and Permeability Tensors. *Phys. Rev. Lett.* **90**, 5 (2003).

4. A. Poddubny, I. Iorsh, P. Belov, and Y. Kivshar: Hyperbolic metamaterials. *Nat. Photonics* **7**, 958 (2013).

5. E. E. Narimanov and A. V Kildishev: Naturally hyperbolic. *Nat. Photonics* **9**, 214 (2015).

6. L. Li, L. Sun, J. S. Gomez-Diaz, N. L. Hogan, P. Lu, F. Khatkhatay, W. Zhang, J. Jian, J. Huang, Q. Su, M. Fan, C. Jacob, J. Li, X. Zhang, Q. Jia, M. Sheldon, A. Alù, X. Li, and H. Wang: Self-assembled epitaxial Au-oxide vertically aligned nanocomposites for nanoscale metamaterials. *Nano Lett.* **16**(6), 3936 (2016).

7. J. Huang, X. Wang, X. L. Phuah, P. Lu, Z. Qi, and H. Wang: Plasmonic Cu nanostructures in ZnO as hyperbolic metamaterial thin films. *Mater. Today Nano* **8**, 100052 (2019).

8. Z. Chen, R. Gao, R. Xu, Y. Lee, X. Zhang, J. Yao, and L. W. Martin: Self-Assembled, Nanostructured, Tunable Metamaterials via Spinodal Decomposition. *ACS Nano* **10**, 10237 (2016).

9. S. Misra, L. Li, D. Zhang, J. Jian, Z. Qi, M. Fan, H. Chen, X. Zhang, and H. Wang: Self-Assembled Ordered Three-Phase Au – BaTiO 3 – ZnO Vertically Aligned Nanocomposites Achieved by a Templating Method. *Adv. Mater.* **31**(7), 1806529 (2018).

10. D. H. Kim, X. Y. Sun, N. M. Aimon, J. J. Kim, M. J. Campion, H. L. Tuller, L. Kornblum, F. J. Walker, C. H. Ahn, and C. A. Ross: A Three Component Self-Assembled Epitaxial

Nanocomposite Thin Film. *Adv. Funct. Mater.* **25**, 3091 (2015).

11. S. Misra, D. Zhang, Z. Qi, D. Li, J. Lu, H. Chen, and H. Wang: Morphology Control of Self-Assembled Three-Phase Au-BaTiO3−ZnO Hybrid Metamaterial for Tunable Optical Properties. *Cryst. Growth Des.* **20**(9), 6101 (2020).

12. N. Zhou, X. Xu, A. T. Hammack, B. C. Stipe, K. Gao, W. Scholz, and E. C. Gage: Plasmonic near-field transducer for heat-assisted magnetic recording. *Nanophotonics* **3**(3), 141 (2014).

13. W. A. Challener, C. Peng, A. V. Itagi, D. Karns, W. Peng, Y. Peng, X. Yang, X. Zhu, N. J. Gokemeijer, Y. T. Hsia, G. Ju, R. E. Rottmayer, M. A. Seigler, and E. C. Gage: Heat-assisted magnetic recording by a near-field transducer with efficient optical energy transfer. *Nat. Photonics* **3**(4), 220 (2009).

14. M. H. Kryder, E. C. Gage, T. W. Mcdaniel, W. A. Challener, R. E. Rottmayer, G. Ju, Y. Hsia, and M. F. Erden: Heat Assisted Magnetic Recording. *Proc. IEEE* **96**(11), 1810 (2008).

15. U. Guler, J. C. Ndukaife, G. V. Naik, A. G. A. Nnanna, A. V. Kildishev, V. M. Shalaev, and A. Boltasseva: Local heating with lithographically fabricated plasmonic titanium nitride nanoparticles. *Nano Lett.* **13**(12), 6078 (2013).

16. L. R. Hirsch, R. J. Stafford, J. A. Bankson, S. R. Sershen, B. Rivera, R. E. Price, J. D. Hazle, N. J. Halas, and J. L. West: Nanoshell-mediated near-infrared thermal therapy of tumors under magnetic resonance guidance. *Proc. Natl. Acad. Sci. U. S. A.* **100**(23), 13549 (2003).

17. D. P. O'Neal, L. R. Hirsch, N. J. Halas, J. D. Payne, and J. L. West: Photo-thermal tumor ablation in mice using near infrared-absorbing nanoparticles. *Cancer Lett.* **209**(2), 171 (2004).

18. Z. Bi, O. Anderoglu, X. Zhang, J. L. MacManus-Driscoll, H. Yang, Q. Jia, and H. Wang: Nanoporous thin films with controllable nanopores processed from vertically aligned nanocomposites. *Nanotechnology* **21**, 285606 (2010).

19. D. Zhang, Z. Qi, J. Jian, J. Huang, X. L. Phuah, X. Zhang, and H. Wang: Thermally Stable Au−BaTiO3 Nanoscale Hybrid Metamaterial for High-Temperature Plasmonic

Applications. *ACS Appl. Nano Mater.* **3**, 1431 (2020).

20. Y. Shen: Carbothermal synthesis of metal-functionalized nanostructures for energy and environmental applications. *J. Mater. Chem. A* **3**(25), 13114 (2015).

21. K. Kodera, I. Kusunoki, and S. Shimizu: Dissociation Pressures of Various Metallic Oxides. *Bull. Chem. Soc. Jpn.* **41**, 1039 (1968).

22. E. a. Secco: Decomposition of zinc oxide. *Can. J. Chem.* **38**, 596 (1960).

23. J. B. Wagner, P. L. Hansen, A. M. Molenbroek, H. Topsøe, B. S. Clausen, and S. Helveg: In situ electron energy loss spectroscopy studies of gas-dependent metal - Support interactions in Cu/ZnO catalysts. *J. Phys. Chem. B* **107**(31), 7753 (2003).

24. J. D. Grunwaldt, A. M. Molenbroek, N. Y. Topsøe, H. Topsøe, and B. S. Clausen: In situ investigations of structural changes in Cu/ZnO catalysts. *J. Catal.* **194**(2), 452 (2000).

25. Z. L. Wang: Zinc oxide nanostructures: Growth, properties and applications. *J. Phys. Condens. Matter* **16**(25), 829 (2004).

26. Y. K. Mishra, V. S. K. Chakravadhanula, V. Hrkac, S. Jebril, D. C. Agarwal, S. Mohapatra, D. K. Avasthi, L. Kienle, and R. Adelung: Crystal growth behaviour in Au-ZnO nanocomposite under different annealing environments and photoswitchability. *J. Appl. Phys.* **112**, 064308 (2012).

27. J. E. Wood, D. B. Williams, and J. I. Goldstein: Experimental and theoretical determination of kAFe factors for quantitative X-ray microanalysis in the analytical electron microscope. *J. Microsc.* **133**(3), 255 (1984).

28. H. Okamoto and T. B. Massalski: The Au-Zn (Gold-Zinc) system. *Bull. Alloy Phase Diagrams* **10**(1), 59 (1989).

29. G. Cliff and G. W. Lorimer: The quantitative analysis of thin specimens. *J. Microsc* **103**, 203 (1975).

30. L. Wang, K. Du, C. Yang, J. Teng, L. Fu, Y. Guo, Z. Zhang, and X. Han: In situ atomic-

scale observation of grain size and twin thickness effect limit in twin-structural nanocrystalline platinum. *Nat. Commun.* **11**(1), 1 (2020).

31. L. Wang, P. Guan, J. Teng, P. Liu, D. Chen, W. Xie, D. Kong, S. Zhang, T. Zhu, Z. Zhang, E. Ma, M. Chen, and X. Han: New twinning route in face-centered cubic nanocrystalline metals. *Nat. Commun.* **8**(1), 1 (2017).

32. S. Sun, D. Kong, D. Li, X. Liao, D. Liu, S. Mao, Z. Zhang, L. Wang, and X. Han: Atomistic Mechanism of Stress-Induced Combined Slip and Diffusion in Sub-5 Nanometer-Sized Ag Nanowires. *ACS Nano* **13**(8), 8708 (2019).

Thermal stability of an ordered three-phase Au-$BaTiO_3$-ZnO vertically aligned nanostructure by both the *ex situ* annealing in air and vacuum conditions, and the *in situ* heating in TEM in vacuum has been demonstrated. The study reveals that the variation of the annealing conditions greatly affects the resulting microstructure and the associated dominant diffusion mechanism.

Keywords:

in situ heating, *ex situ* heating, thermal stability, metamaterial, thin films, vertically aligned nanocomposite

Thermal stability of self-assembled ordered three-phase Au-$BaTiO_3$-ZnO nanocomposite thin films via *in situ* heating in TEM